

Article

XFEM-Based Study of Fatigue Crack Propagation in Rocket Deflector Troughs under Coupled High-Temperature and Impact Conditions

Zhixin Xiong ^{1,*}, Chengyuan Zhu ², Yue Yang ³, Tong Lin ³ and Ruoxuan Li ¹

¹ College of Ocean Science and Engineering, Shanghai Maritime University, Shanghai 201306, China

² Merchant Marine College, Shanghai Maritime University, Shanghai 201306, China

³ Marine Design & Research Institute of China, Shanghai 200011, China

* Correspondence: zxxiong@shmtu.edu.cn

Abstract: This research investigated fatigue crack propagation on the lower surface of rocket deflector troughs in offshore rocket launch platforms. Initially, a numerical model of an offshore rocket launch platform was established using ABAQUS based on the Extended Finite Element Method (XFEM). Subsequently, two variable parameters—the initial crack length and initial tilt angle—were introduced. This research systematically analysed the impact of these parameters on the fatigue crack propagation patterns in both the maximum stress and maximum deformation regions of the deflector channels under the combined conditions of high temperature and impact. Finally, the research indicated that the propagation length of surface cracks in the deflector trough exhibited an initial increase followed by a decrease with the rise in the pre-set inclination angle. Notably, the stable propagation rate of the crack in the region of maximum deformation surpassed that observed in the region of maximum stress. Through meticulous comparative analysis, it was evident that temperature loading significantly exacerbated the initiation and propagation of cracks, particularly in the upper region of the deflector channel's lower surface.

Keywords: offshore rocket deflector troughs; fatigue crack propagation; XFEM; high temperature and impact coupling



Citation: Xiong, Z.; Zhu, C.; Yang, Y.; Lin, T.; Li, R. XFEM-Based Study of Fatigue Crack Propagation in Rocket Deflector Troughs under Coupled High-Temperature and Impact Conditions. *J. Mar. Sci. Eng.* **2024**, *12*, 207. <https://doi.org/10.3390/jmse12020207>

Academic Editor: Vincenzo Crupi

Received: 26 December 2023

Revised: 17 January 2024

Accepted: 21 January 2024

Published: 23 January 2024



Copyright: © 2024 by the authors. Licensee MDPI, Basel, Switzerland. This article is an open access article distributed under the terms and conditions of the Creative Commons Attribution (CC BY) license (<https://creativecommons.org/licenses/by/4.0/>).

1. Introduction

As the frequency of space launch missions continues to rise, the deployment of rocket deflector troughs is increasing correspondingly, introducing inherent structural fatigue challenges. According to the statistics, more than 70% of the damage to marine engineering structures during their service life is caused by fatigue [1]. Consequently, the initiation and propagation of cracks due to structural fatigue have emerged as the primary causes of marine engineering structure failures. In the context of the challenging maintenance conditions of offshore rocket launch platforms, it is imperative to comprehend the trajectory from crack initiation to structural failure within the direct impact zone of rocket plumes on deflectors. This understanding holds significant importance for evaluating the remaining structural life of these platforms, particularly in light of stringent damage tolerance requirements.

The Extended Finite Element Method (XFEM), as an emerging numerical approach for simulating fatigue crack propagation, retains the advantages of traditional finite element methods. It utilises specialised crack tip enrichment functions to model the stress singularity at the crack tip, allowing the crack interface to be independent of the mesh, reducing mesh dependence, and simplifying the treatment of the crack tip refinement [2]. This makes the XFEM an effective and efficient tool for addressing crack growth problems [3–5]. Numerous scholars have conducted in-depth research and experimental extensions on this method. Patzak et al. [6] conducted an in-depth study on the analytical process of the XFEM. Zhang et al. [7] used the Extended Finite Element Method to study the impact of compressive

stress on crack propagation under tension-compression loading, revealing a relationship between crack initiation at the crack tip and compressive stress. Menouillard et al. [8] simulated dynamic crack propagation using the XFEM based on explicit time integration techniques. Fries et al. [9] introduced three horizontally integrated functions explicitly computed to enhance the three-dimensional applicability of the XFEM, proposing a new approach that combines explicit and implicit methods for simulating crack propagation. Daux et al. [10] applied the Extended Finite Element Method to simulate crack branching. Himanshu Pathak et al. [11] used the XFEM to simulate fatigue crack propagation under cyclic thermal loads for three-dimensional linear elastic cracks with different geometries, revealing the robustness and versatility of the XFEM. Loehnert et al. [12] discussed a series of computational issues related to the three-dimensional XFEM, studying the impact of finite deformation theory on crack simulation through numerical examples. Danas et al. [13] used the XFEM to study energy minimisation in the multiple crack propagation of linear elastic solids under quasi-static conditions, proposing an alternative strategy to supplement the implementation and application of gradient descent methods within the XFEM framework.

While conducting in-depth research on the XFEM, many scholars have also applied this method to address practical problems. Through experiments applying compressive stress on notched plates, Fleck et al. [14] found that cracks originated in the residual tensile stress region near the notch root and extended, indicating that fatigue cracks are more prone to propagate under tensile stress conditions. Sahouryeh et al. [15], through experiments, observed the crack propagation behaviour under biaxial compressive stress and found that the size of crack growth was limited, with the propagation direction parallel to the loading direction. Nikfam et al. [16] simulated high-cycle fatigue tests on welded T-joints using the XFEM, validating that the XFEM predictions of crack propagation rate, life, and shape were within a reasonable range of the experimental results, with the fracture morphology of the numerical model consistent with experimental observations. Teng et al. [17] utilised the XFEM to investigate the influence of different micro-defects on macro-crack propagation. The study results not only demonstrated the XFEM's ability to accurately capture the stress intensity factors at the macro-crack and micro-defect crack tips but also revealed that the impact of micro-defects on the macro-crack propagation path changed with their position and size.

Based on simulated rocket plume parameters, this study employed numerical simulation to investigate the influence of the rocket plume on the launch platform, especially the deflector, during rocket launch. The simulation incorporated both high-temperature and exhaust plume impact load coupling, considering the effects of temperature loads on the mechanical properties of the deflector's metallic material. The force conditions on the deflector during the rocket's takeoff phase were realistically simulated. Finally, the XFEM was applied to analyse the fatigue crack propagation on the lower surface of the rocket deflector with pre-existing initial cracks. This study primarily focuses on the direction, initiation length, and fatigue propagation rate of cracks in rocket deflectors with initial cracks caused by fatigue damage or material defects during their subsequent operational service. The obtained results will serve as a reference for the safety performance design of maritime rocket deflectors.

2. Models and Environmental Parameters

2.1. Rocket Launch Platform Model

The research in this paper focuses on the lower surface of a rocket deflector trough subjected to direct impingement from the rocket plume, as illustrated in the overall model of an offshore rocket launch platform shown in Figure 1a.

Given that the high-temperature and high-speed airflow during rocket launches primarily affects the launch area of the platform (the main body of the deflector trough and the connected upper deck region), and considering the symmetrical distribution of the deflector trough, the right side of the deflector trough was selected as the representation

area for computational results to simplify the visualisation, as illustrated in Figure 1b. During a rocket launch, the plume jet traverses the deflector trough inlet positioned at the centre of the launch deck, exerting a direct impact on the deflector trough beneath the deflection hole. Subsequently, it follows the guidance of the deflector’s lower surface, ultimately exiting from the openings at both ends of the deflector. The dimensions of the deflector trough are illustrated in Figure 2.

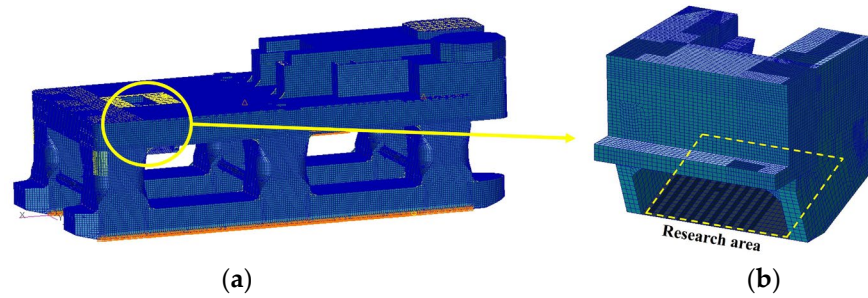


Figure 1. Schematic diagram of offshore rocket launch platform (a) and deflector trough model (b).

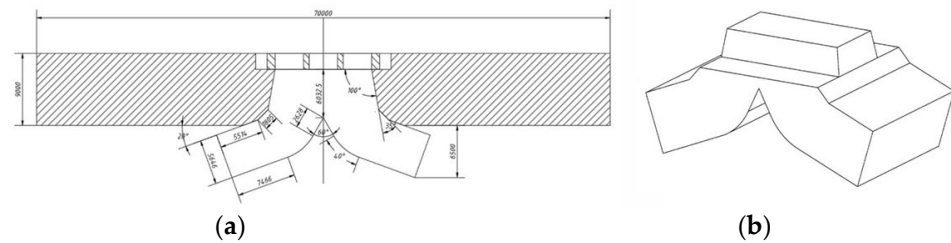


Figure 2. Diagram of deflector dimensions; (a) Overall dimensions diagram of the rocket deflector; (b) Overall profile diagram of the rocket deflector.

2.2. Environmental Load Parameters

The external environmental parameters of the deflector are primarily divided into temperature parameters and exhaust plume impact load parameters. The conventional method to ensure the structural safety of the rocket deflector is to install heat insulation materials on the surface of the deflector, which can significantly reduce the temperature of the metal structure directly exposed to the rocket plume. By incorporating sensors beneath the insulating layer on the lower surface of the deflector, it becomes possible to capture data regarding temperature variations and exhaust plume impact loads during the initial 1.1 s of a rocket launch. Figures 3 and 4 illustrate the numerical values of temperature and impact force at specific moments, visually representing these critical parameters.

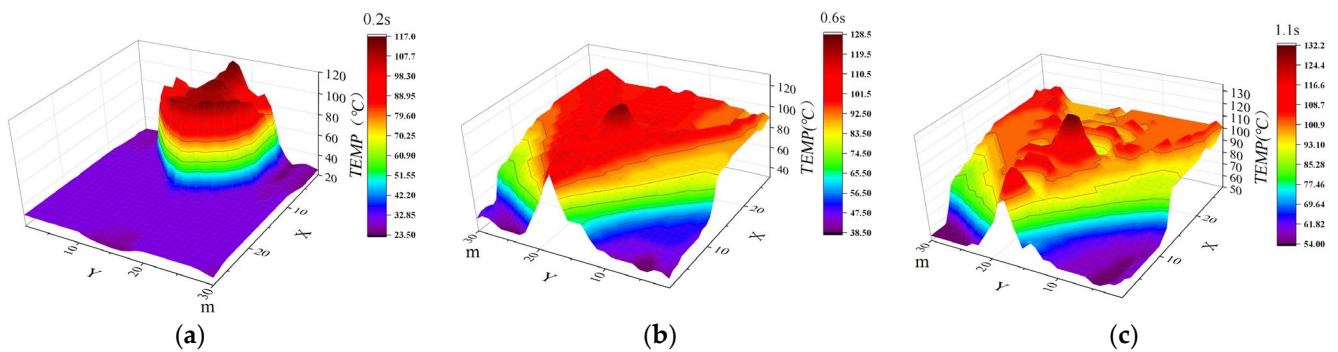


Figure 3. Temperature contour plot: (a) 0.2 s, (b) 0.6 s, (c) 1.1 s.

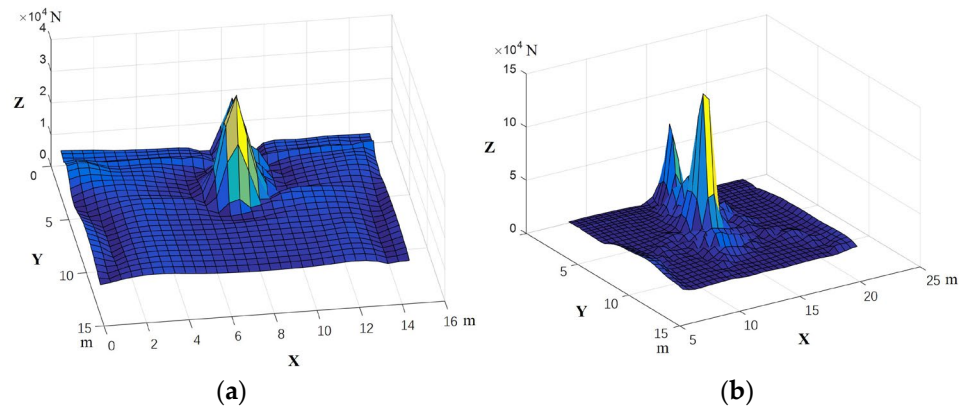


Figure 4. Impact force load cloud map; (a) 0.2 s; (b) 1.1 s.

The boundary conditions for the overall model were defined as an air environment with a pressure of 101,325 Pa and an ambient temperature of 20 °C. There was no heat exchange between the deflector and the external environment. The deflector walls were treated as no-slip surfaces. The boundary constraints were applied to both the symmetry planes of the deflector and the region where the deflector is connected to the upper deck of the platform, involving fixed displacement and rotation. The material chosen for the rocket deflector was grade E ordinary shipbuilding steel. The chemical composition of this steel is: C ≤ 0.17%, Mn ≤ 1.4%, Si ≤ 0.35%, P ≤ 0.035%, S ≤ 0.035%, Al ≥ 0.015%. It is crucial to note that the increase in temperature not only diminishes the elastic modulus of the metal material but also attenuates its yield strength [18]. Consequently, both these material properties are dynamically adjusted with temperature variations [19], as comprehensively outlined in Table 1 [20]. The temperature referenced for the fracture mechanics properties of the deflector metal material is above 200 °C. In comparison, this study’s maximum temperature on the lower surface was 132.2 °C. The actual temperature of the metal is lower than this, because this study measured the temperature on the backside of the insulation material. The fracture mechanics properties of the deflector material were set using room temperature parameters, as detailed in Table 2 [21].

Table 1. Elastic modulus and yield strength of grade E shipbuilding steel at various temperatures.

Temperature (°C)	Elastic Modulus (10 ⁵ MPa)	Yield Strength (MPa)
16	2.032	299.0
200	1.950	245.8
250	1.930	229.0

Table 2. The fracture mechanics properties of grade E steel at room temperature (20 °C).

G_{IC} (N/mm)	C	m	ΔK_{th} (N/mm ^{3/2})
80.0330	2.2644×10^{-16}	4.1987	225.7000

The material parameters c_1 and c_2 were used to judge the crack from absence to presence and were taken as 0.5 and −1, respectively. The parameters c_3 and c_4 were related to the material’s intrinsic properties and were taken as 3.74×10^{-5} and 2.0994, respectively.

3. Simulation Calculation Equations

3.1. XFEM

The fundamental idea of the XFEM [22] is the method of unit decomposition, which introduces enriched functions into the displacement modes of FEM to characterise strong discontinuities in the displacement field:

$$u^h = \sum_i N_i(x)u_i + \varphi(x) \tag{1}$$

where u^h is the discontinuous displacement field; standard finite elements apply the shape function; u_i represents the degrees of freedom of regular nodes; and $\varphi(x)$ represents the enriched approximation functions associated with the method of unit decomposition.

When applying the XFEM to solve crack propagation, the software divides the material elements into three categories: standard elements, penetrating elements, and crack tip elements. For the elements experiencing crack propagation, discontinuous shape functions can be introduced to control the displacement:

$$\begin{cases} u_{xfem}(x) = u_{fem}(x) + u_{step}(x) + u_{tip}(x) \\ u_{fem}(x) = \sum_{i \in I} N_i(x)u_i \\ u_{step}(x) = \sum_{i \in I_{step}} N_i(x)H(x)a_i \\ u_{tip}(x) = \sum_{i \in I_{tip}} N_i(x)F(x)b_i \end{cases} \tag{2}$$

In the equation above, $u_{xfem}(x)$ represents the approximate displacement field of the extended finite element; $u_{fem}(x)$ represents the approximate displacement field of the standard finite element; $u_{step}(x)$ represents the approximate displacement field of the penetrating element crack; $u_{tip}(x)$ represents the approximate displacement field of the crack in the crack tip element; I is the set of all nodes in the solution domain; I_{step} is the set of nodes penetrated by the crack; I_{tip} is the set of nodes affected by the crack tip region; $H(x)$ is the step function for the penetrating element; $F(x)$ is the enrichment function for the crack tip element; a_i represents the degrees of freedom associated with enriched nodes related to the jump discontinuity; and b_i represents the degrees of freedom associated with enriched nodes related to the crack tip approximation function.

3.2. Crack Propagation Criteria

The Paris equation can represent the initiation and propagation of fatigue cracks [23]:

$$\frac{da}{dN} = c_3(\Delta G)^{c_4} \tag{3}$$

In the equation above, c_4 represents material-related constants.

The Paris law in the simulation associates the crack propagation rate with the energy release rate (ΔG) at the crack tip. $\Delta G = G_{max} - G_{min}$, G_{max} represents the strain energy release rate corresponding to the maximum load on the structure and the strain energy release rate corresponding to the minimum load on the structure.

The Paris law operates within the bounds of G_{thresh} and G_{pl} , where fatigue cracks do not propagate below the former and rapidly propagate until failure above the latter. The intermediate region between the two represents a stable crack propagation zone for fatigue cracks.

3.3. Damage Initiation Criteria and Evolution Criteria in ABAQUS

(1) Damage Initiation Criterion: Maximum Principal Stress Criterion (Maxps Damage)

$$f = \left\{ \frac{\langle \sigma_{max} \rangle}{\sigma_{max}^0} \right\} \tag{4}$$

When $1.0 < f < 1.0 + f_1$ within the tolerance range, damage initiates. Here, f_1 is the tolerance, typically set to 0.05; σ_{\max}^0 is the critical maximum principal stress value; and $\langle \sigma_{\max} \rangle$ signifies

$$\begin{cases} \langle \sigma_{\max} \rangle = 0, \sigma_{\max} < 0 \\ \langle \sigma_{\max} \rangle = \sigma_{\max}, \sigma_{\max} \geq 0 \end{cases} \quad (5)$$

The above expression implies that no damage initiation occurs in the element with a penetrating crack under pure compressive loading conditions.

(2) Damage Evolution Criterion: Energy-Based Damage Evolution Criterion

In ABAQUS, the overall damage of a structure is represented by D , with an initial value of 0. If a damage evolution model is defined, the value of D increases after the model undergoes further loading, gradually evolving towards 1. ABAQUS's damage evolution law describes the degradation rate of material stiffness in each cycle once the corresponding initiation criteria are met. For ductile materials, ABAQUS assumes that stiffness degradation can be modelled using a scalar damage variable D . Within any given analysis cycle, the stress tensor in the material is determined by the scalar damage equation:

$$\sigma = (1 - D)\bar{\sigma} \quad (6)$$

The equation σ represents the effective (undamaged) stress tensor present in the material during the current incremental calculation when no damage has occurred. When D equals 1, it indicates that the material has lost its load-bearing capacity, and damage has occurred [24].

(1) Linear Evolution Damage Criterion:

$$D = \frac{s_m(s_{\max} - s_0)}{s_{\max}(s_m - s_0)} \quad (7)$$

In the equation above, $s_m = \frac{2G}{F}$, F is the effective traction measured in MPa, and G is the energy released upon damage measured in J.

(2) Exponential Evolution Damage Criterion:

$$D = \int_{s_0}^{s_m} \frac{F ds}{G - G_0} \quad (8)$$

In the equation above, G_0 is the energy release at the onset of damage measured in J, and s is the effective displacement measured in mm.

4. Experimental Validation of the Effectiveness of the Simulation Method

4.1. Experimental Setup

The material used for the fatigue crack propagation experiment was the GH4133B alloy, in the form of standard CT specimens. The stress ratio for the fatigue experiment was set to 0.02 ($R = 0.02$), and a sinusoidal wave with a frequency of 5 Hz was employed as the experimental loading frequency. The tensile stress direction was set as symmetrically reversed [25].

The measurement method for fatigue crack propagation was as follows: After subjecting the specimen to a certain number of cyclic stress loadings, the test machine was temporarily halted. Subsequently, the specimen's crack was examined utilising an electron microscope, with images of the crack tip captured. These images were then juxtaposed with prior observation results to trace the path of fatigue crack propagation, concurrently documenting the associated cycle counts. The specimen parameters are shown in Table 3 and Figure 5, and the tested specimen is shown in Figure 6.

Table 3. Specimen parameters.

Specimen Number	Symmetric Load (P/kN)	Specimen Thickness (W/mm)
1	7	6.8
2	6.5	6.8
3	8.5	6.4
4	8.8	6.8

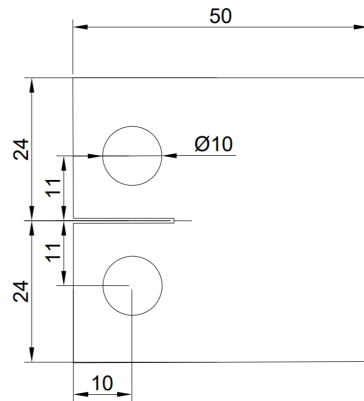


Figure 5. Specimen dimensions and loading configuration.



Figure 6. Experimental specimen.

4.2. Comparison between Experimental Data and Simulation Data

The stress cycle counts obtained through experimental measurements and simulated by the Extended Finite Element Method when the crack propagated to a length of 15 mm are presented in Table 4. The relationship between the crack length (a) and the number of cycles (N) for specimens measured through experimental methods and simulated using the XFEM is illustrated in Figure 7.

Table 4. Comparison of experimental and simulation results.

Specimen Number	Number of Cycles in the Experimental Method (N/Cycle)	Number of Cycles in the Simulation Method (N/Cycle)	Relative Error (%)
1	135,375	140,515	3.80
2	179,672	175,050	2.57
3	50,080	50,975	1.79
4	70,806	71,575	1.09

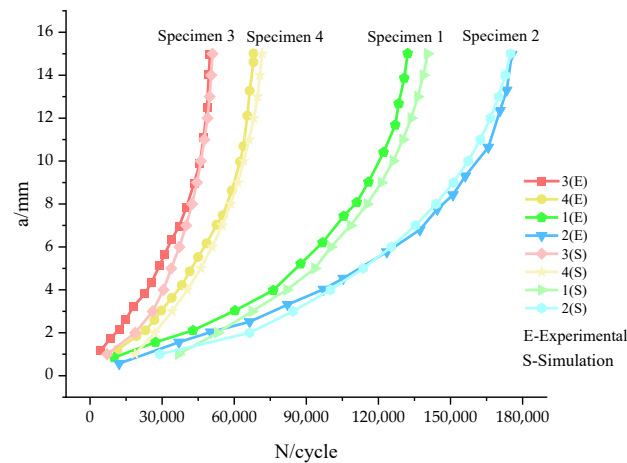


Figure 7. Comparison of experimental and simulation results.

Reviewing Table 4, it becomes apparent that the maximum error in the number of cycles measured by the two methods was 3.8%. Figure 7 illustrates that the crack propagation patterns of the specimens obtained through both methods generally aligned under equivalent thickness and load conditions. The observed trend indicated an increment in crack propagation rates with the number of load cycles, affirming the reliability of XFEM simulation.

5. Numerical Results and Discussion

5.1. XFEM Simulation Approach for Fatigue Crack Growth

This paper employed the XFEM to simulate the numerical growth process of cracks. The XFEM, by introducing additional shape functions into the finite element mesh, can handle the extension of cracks more naturally. In the calculation of crack propagation, the XFEM employs the concept of unit decomposition to introduce specific functions relevant to the problem into the approximation space, ensuring the convergence of results [26]. The level set method is a numerical technique within the XFEM used to determine the position of the internal interface of cracks and to track the growth of cracks. Any internal interface can be represented using its zero-level set function [27,28].

In the simulation, the release of nodes at the crack tip was based on ABAQUS damage initiation and evolution criteria. The fracture energy in the crack tip region accumulated as the load cycled continuously. When the cumulative fracture energy at the crack tip nodes reached a specific threshold, the XFEM released the fracture energy at the tip, and this released energy was used to initiate a new crack, simulating the extension of the crack. ABAQUS abandons the coupling issues introduced by two shape functions, making it unable to simulate branching cracks. However, the XFEM, utilising the unit decomposition and level set methods, can accurately simulate the extension of a single crack. Therefore, in this paper, crack propagation refers to the growth and elongation of cracks caused by cyclic loading and does not include an increase in the number of cracks.

The growth of the crack in each numerical step was determined by monitoring the stress intensity factor range at the crack tip [29]. Using empirical relationships like the Paris law, the crack growth rate was associated with changes in the stress intensity factor, allowing for the crack growth calculation in each step. This ensured that the XFEM can simulate the actual growth behaviour of cracks under fatigue loading.

5.2. Crack Area Configuration

The crack locations were chosen based on the stress–strain calculation results of the deflector’s lower surface. Two positions were selected, one corresponding to the maximum stress and the other to the maximum strain. Figure 8 indicates the specific locations of the cracks along with the results of stress/strain calculations. Position A corresponds to the location with the maximum stress, as shown in part (a). Position B corresponds to the

location with the maximum strain, as indicated in part (b). The region circled in yellow represents the area designated for pre-inserted cracks. The width of the lower surface of the deflector plate was 20 m. According to the design requirements for the launch platform, the crack size could not exceed 5‰ of the deflector plate width. This paper conducted simulations under the worst-case-scenario assumption; hence, the initial crack length was set to 100 mm.

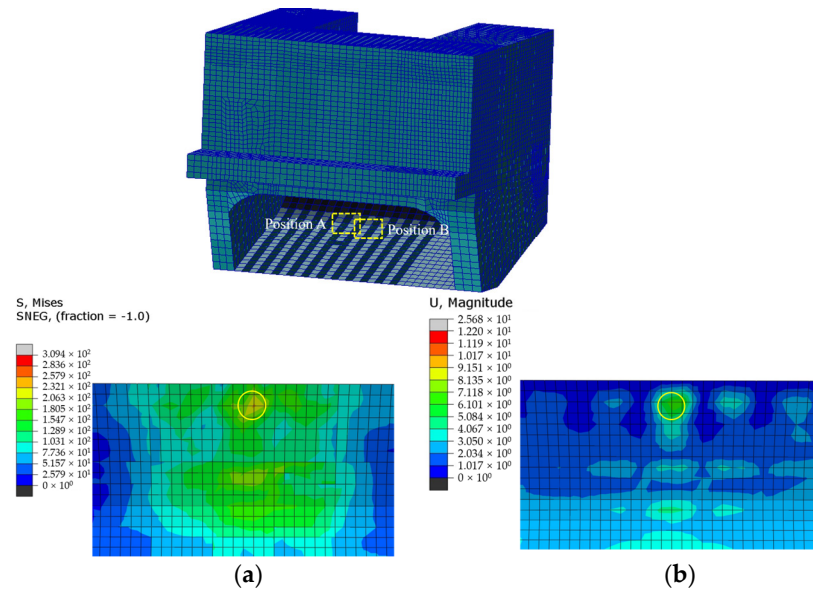


Figure 8. Schematic diagram of operating condition zones; (a) Condition A: Cracks are positioned at the locations of maximum stress; (b) Condition B: Cracks are positioned at the locations of maximum deformation.

Considering that the crack propagation on the lower surface of the deflector occurred only in localised regions, a “shell-to-solid” coupling theory based on ABAQUS [30] was adopted. Figure 9 illustrates the shell–solid coupling principle. In this approach, the localised regions where cracks must pre-exist are configured as three-dimensional solids. In contrast, the overall model region is kept as a two-dimensional shell. This configuration was implemented to simplify the computational process. The form of the crack was characterised as a penetrating crack.

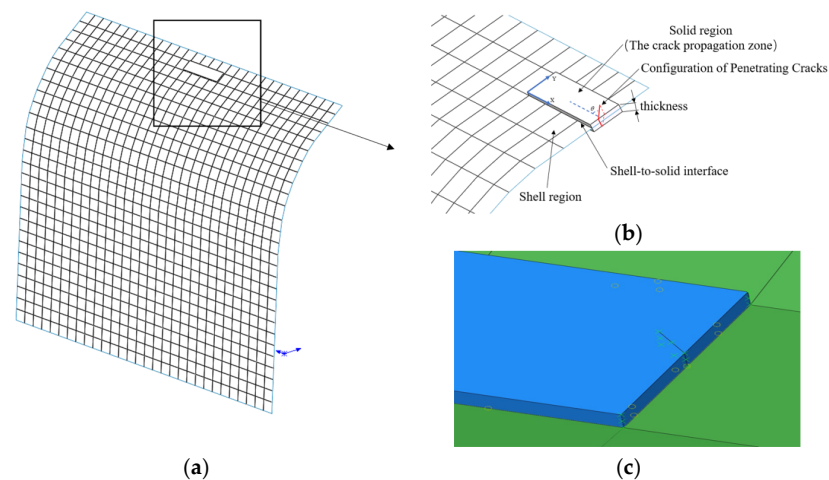


Figure 9. Shell-to-solid coupling schematic diagram; (a) Overall; (b) Local detailed illustration; (c) Crack configuration.

The cracks studied in this paper were penetrating cracks that vertically traversed the lower plate of the deflector groove. The plane coordinate system selected for measuring the initial crack's inclination angle was located on the plane in the region where the crack was present. Figure 9b,c illustrates the configuration of penetrating cracks and the establishment of the coordinate system referenced by the inclination angle of the crack.

5.3. Crack Propagation Direction

The pre-inserted cracks on the lower surface of the rocket deflector experienced various types of stress, including tensile stress, compressive stress, torsional stress, and shear stress. Due to the non-uniformity in the motion of the rocket plume flow field, there were variations in the temperature and exhaust plume impact loads, both in terms of direction and magnitude, across different regions of the lower surface of the deflector trough. As a result, cracks at different positions and inclinations experienced differences in the magnitude and direction of the principal stress. Figures 10 and 11 depict schematic diagrams illustrating the inclination and propagation of pre-inserted cracks under the propagation scenario for two operational conditions, both occurring within the same number of load cycles. In the figures, the X-axis direction corresponds to 0° , and the Y-axis direction to 90° . The counterclockwise direction represents an increase in inclination. For clarity, the crack represented by the thick line in the figure is the initially pre-set crack in the deflector groove. In contrast, the crack represented by the thin line is the newly formed portion resulting from the fatigue-induced crack propagation of the pre-set initial crack.

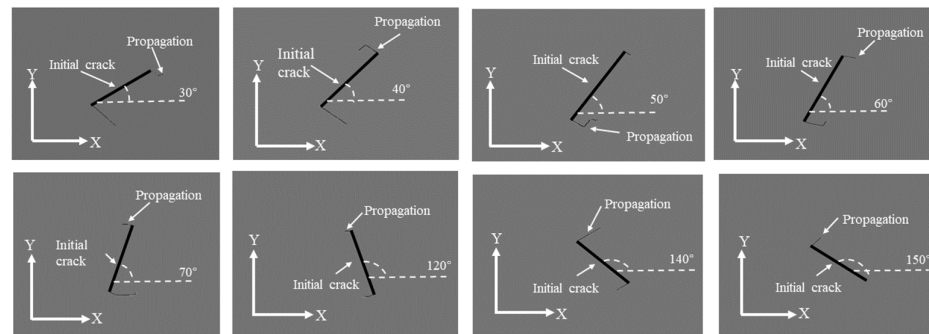


Figure 10. The crack propagation results under different pre-set inclinations for operational condition A.

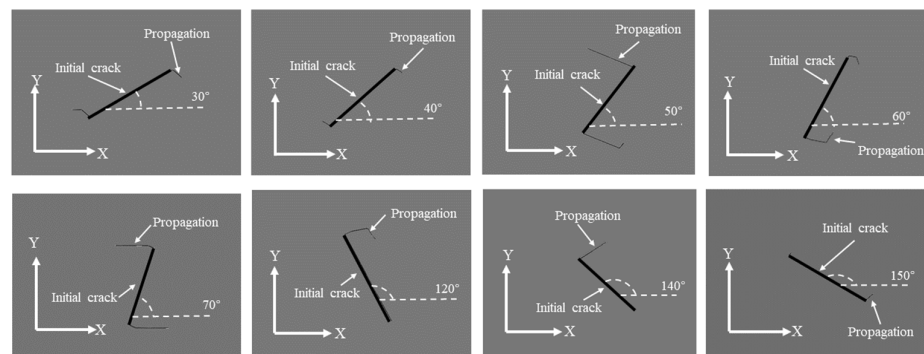


Figure 11. The crack propagation results under different pre-set inclinations for operational condition B.

The deformation coefficients in the resulting figures were set to 0 for ease of observing the crack extension. According to the crack propagation results of the pre-inserted cracks on the lower surface of the deflector trough under the two operating conditions, it was evident that with the continuous increase in the pre-set inclination angle, the crack propagation length exhibited a trend of initially increasing and then decreasing. The maximum crack propagation length was attained when the inclination angle approached 70° . Comparing the crack propagation lengths in the two operating conditions, it was observed that under the

same inclination angle and number of stress cycles, the crack propagation length in the region of maximum deformation was generally greater than in the region of maximum stress.

Figure 12 illustrates the relationship between the crack propagation direction and the location of the maximum principal stress at the crack tip. The black line represents the initially pre-set crack, while the thin blue line represents the newly formed portion due to fatigue crack extension. The green arrow indicates the direction of crack propagation, and the numbers above the arrows represent the element numbers penetrated by the crack. For example, “①” represents the number of the first unit cell penetrated by the crack. The red dots represent the positions of the maximum principal stress due to stress concentration when the crack penetrates each element, and the yellow dots represent the positions of the secondary stress (stress values just below the maximum principal stress) due to stress concentration when the crack penetrates each element. The numbers before the stress values correspond to the element numbers. For example, “1) 418 MPa” corresponds to a red value, and the digit “1” before the numerical value indicates the maximum stress value at the crack tip and its location when the crack penetrates the first unit cell. The adjacent pairs of points arranged side by side in the figure indicate that both the maximum principal stress and secondary stress occurred at that point before and after the crack penetration.

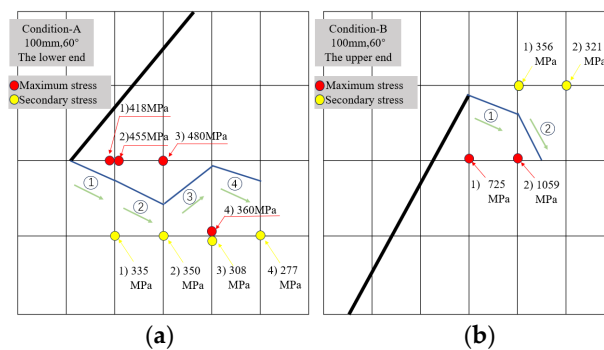


Figure 12. Diagram of crack propagation direction and principal stress locations. (a) Diagram of crack propagation in the lower region, (b) Diagram of crack propagation in the upper region.

Figure 12 shows that as the crack propagated within an element, stress concentrations occurred at the nodes along its advancement direction. The node’s position with the maximum stress determined the deviation direction of the crack tip within that element. Simultaneously, the position and stress magnitude of secondary stress nodes influenced the deflection angle of the crack propagation.

The combined analysis of crack propagation trends under both operating conditions revealed that, under certain pre-set inclination angles (50°, 60°), crack propagation was not solely oriented towards increasing the length of the crack. After a certain distance of cracking, the crack trajectories at the upper and lower ends, or one of them, tended to extend into the region where the fracture had already occurred. This indicates a tendency to detach the surrounding structure from the lower surface of the deflector. If this trend of crack propagation continued, it would compromise the integrity of the deflector trough structure, reducing the strength of the lower surface structure. Simultaneously, detached fragments of the overall structure would be ejected with high kinetic energy, accompanying the plume flow field within the deflector trough. This could result in secondary damage to the deflector trough and other structures, posing a potential threat to the rocket engine. Therefore, particular attention should be given to the 50° and 60° inclination cracks originating from fatigue damage on the lower surface of the rocket deflector trough.

5.4. Minimum Initial Crack Length for Crack Propagation

Table 5 shows that the number of load cycles required for the initiation and propagation of pre-inserted cracks at different inclinations exhibited an overall trend of initially decreasing and then increasing with the increase in the inclination angle. For condition A,

the minimum initiation and propagation angle was 50°, while for condition B, the minimum initiation and propagation angle was 60°. In this section, the minimum initiation and propagation angles obtained from Table 5 for the two operating conditions were taken as pre-set angles to investigate the minimum initiation and propagation lengths of cracks at these two angles under their respective conditions.

Table 5. Crack initiation cycle numbers at different pre-set inclinations.

Inclination	30°	40°	50°	60°	70°	120°	140°	150°
Condition A	2317	6221	609	2191	1465	3013	5761	19,992
Condition B	32,217	31,647	1251	266	2719	3125	1435	23,495

This section explores the minimum initial length required for the continued expansion of the initial crack on the lower surface of the deflector groove. In this section, the variable being changed was the length of the initially pre-set crack on the rocket deflector groove. Regarding the practical scenario, within the service life cycle of a rocket launch platform, no more than 60,000 rocket launch missions and experiments will be undertaken. Therefore, with 60,000 load cycles as the upper limit, if no fatigue propagation occurs in the initial crack after 60,000 load cycles, it is considered that a crack of that length will not continue to propagate. This section also uses this criterion to determine whether the crack is propagating.

With the increase in the initial length of pre-existing cracks, the rate of fracture energy accumulation at the crack tip accelerates, reducing the number of stress cycle repetitions required for crack initiation. Figure 13 illustrates that, under condition A, the minimum crack initiation length was approximately 40 mm, whereas under condition B, it was around 20 mm. In the region of maximum stress, the number of cycles required for crack initiation is highly sensitive to changes in the initial crack length. As the initial crack length increases, the initiation cycles for cracks located at the point of maximum stress sharply decrease. In the region of maximum deformation, the increase in the initial crack length has a relatively weak impact on reducing the crack initiation cycles. The overall decrease remains relatively stable. From the figure, it can be observed that when the initial crack length exceeded 85 mm, cracks pre-existing in the region of maximum stress exhibited a faster crack initiation rate, whereas, for lengths below 85 mm, cracks situated in the region of maximum deformation demonstrated a faster initiation rate.

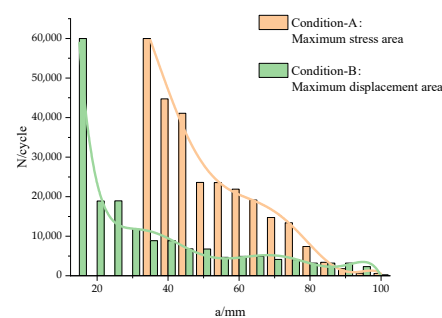


Figure 13. Load cycle number diagram before initiation of cracks with different lengths.

5.5. Crack Propagation Rate

Figure 14 shows that in both conditions, the crack propagation rate exhibited significant fluctuations and abrupt changes during the early stages of fatigue crack propagation. These fluctuations are attributed to variations in the crack propagation mechanism and changes in stress amplitude. Additionally, since ABAQUS cannot simulate stress concentration within the interior of elements, every crack propagation was bound to penetrate one or more element bodies completely, leading to fluctuations in the calculated crack propagation

rates. However, with an increase in the number of stress cycles, both the crack propagation rate and fluctuations eventually stabilised.

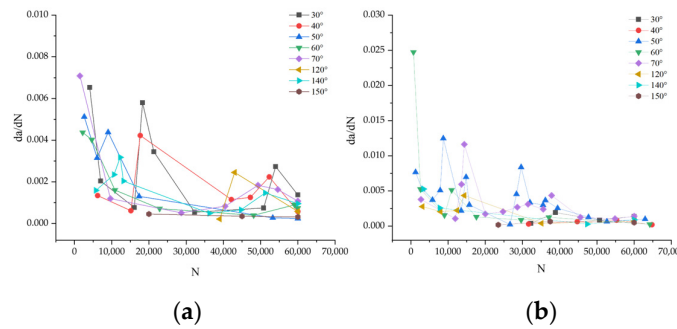


Figure 14. Crack propagation rate chart; (a) Condition A; (b) Condition B.

By comparing the two operating conditions, it can be observed that the fluctuation amplitude of the crack propagation rate under condition A was approximately 0.0063, which is smaller than the fluctuation amplitude under condition B (0.022). Figure 14 shows that the crack propagation rate in the region of maximum deformation was higher than that in the region of maximum stress. Simultaneously, the crack in the region of maximum deformation reached the stable propagation stage faster compared to the region of maximum stress. This is because the region of maximum stress undergoes larger stress gradient changes during the loading process, leading to significant differences in stress gradients at the ends of the crack. This results in a smaller stress ratio, exacerbating the amplitude variations in cyclic stress, and thereby prolonging the time for the crack propagation rate to stabilise.

5.6. Analysis of the Influence of High-Temperature Environment on Fatigue Life

To investigate the impact of temperature on the fatigue crack propagation of the lower surface of the deflector trough, it was necessary first to study the influence of temperature loads on the stress distribution of the lower surface.

Figure 15 presents the stress contour map of the lower surface of the rocket deflector at a specific moment under the influence of temperature loads or without them. As shown in the diagram, under the action of a single impact force, the maximum stress on the lower surface of the deflector was located in the middle region directly impacted by the tail flame, with a peak value of 175 MPa. However, when coupled with temperature loads, the concentration of stress on the lower surface increased, and it was distributed more in the upper-middle region. The maximum stress value rose to 198 MPa, representing an increase of approximately 13%.

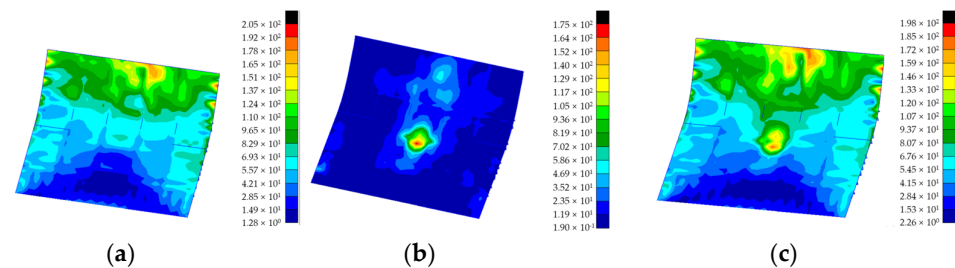


Figure 15. (a) Temperature load, (b) Impact force load, (c) Coupled load.

According to Table 6, it can be observed that in the early stages of rocket launch, as the launch time progressed, the impact of coupled temperature load on the increase in stress on the lower surface of the deflector trough exhibited a gradually decreasing trend. When the rocket tail flame jet’s distribution state stabilised on the deflector trough’s lower surface, the temperature load increased the maximum stress value on the lower surface of the deflector

trough, which was subjected only to a single impact force, by approximately 10%. Through Figure 15, it can be observed that temperature load altered the stress distribution on the lower surface of the deflector under the action of a single exhaust plume impact load, causing the concentration of stress to shift from the central region directly impacted by the rocket’s tail flame to the upper-middle region. The maximum stress value induced by the temperature load (205 MPa) was greater than the maximum stress values under the exhaust plume impact load alone (175 MPa) and the coupled load (198 MPa). This indicates that the coupling of temperature and exhaust plume impact loads decreases the maximum stress on the lower surface, thereby enhancing the fatigue life of the deflector’s lower surface.

Table 6. Influence of temperature load.

T/s	0.14	0.28	0.42	0.70	0.85	0.98	1.1
Impact Force Load (MPa)	10.3	32.4	70.0	129.0	157	183.0	175.0
Coupled Load (MPa)	221.0	201.0	174.0	182.0	185.0	190.0	198.0
Impact of Temperature Load (%)	95.3	83.9	60.0	29.1	15.1	3.7	11.6

The impact of temperature load = (coupled load – exhaust plume impact load)/coupled load.

Applying the S-N curve method for calculating the crack initiation life on the lower surface of the deflector revealed that cyclic loading from a single impact force alone did not lead to structural fatigue failure on the lower surface. Consequently, there was no initiation or propagation of cracks on the lower surface of the deflector under the influence of an exhaust plume impact load alone.

6. Conclusions

This paper, based on the XFEM, draws the following conclusions through a study on fatigue crack propagation on the lower surface of an offshore rocket deflector:

- (1) Under the coupling effect of high temperature and impact, the length of fatigue crack propagation on the lower surface of the rocket deflector exhibits an increasing trend with the increase in the pre-set tilt angle, followed by a decrease when the tilt angle exceeds 70°. The maximum crack propagation length is reached when the tilt angle approaches 70°.
- (2) The node’s position with the maximum circumferential stress at the crack tip will determine the crack propagation direction. Simultaneously, the position and magnitude of secondary stress nodes will influence the deflection angle of crack propagation.
- (3) Compared to the exhaust plume impact load alone, the coupled temperature load not only increases the maximum stress on the lower surface of the deflector by approximately 10% but also shifts the stress concentration region from the central area directly impacted by the rocket’s tail flame to the upper-middle region. This, in turn, promotes the initiation and propagation of cracks on the lower surface of the deflector.

Author Contributions: Conceptualization, Z.X. and Y.Y.; methodology, Z.X.; software, C.Z.; validation, T.L.; formal analysis, C.Z.; investigation, R.L.; resources, Z.X.; data curation, T.L. and Y.Y.; writing—original draft preparation, Z.X. and C.Z.; writing—review and editing, Z.X., C.Z. and Y.Y.; visualization, R.L. All authors have read and agreed to the published version of the manuscript.

Funding: This research received no external funding.

Institutional Review Board Statement: Not applicable.

Informed Consent Statement: Not applicable.

Data Availability Statement: The data presented in this study are available on request from the corresponding author.

Acknowledgments: We are grateful for the software support from the Marine Design and Research Institute of China.

Conflicts of Interest: The authors declare no conflicts of interest.

References

1. Cui, W.; Cai, X.; Leng, J. A state-of-the-art review for the fatigue strength. *J. Ship Mech.* **1998**, *4*, 63–81.
2. Bergara, A.; Dorado, J.I.; Martín-Meizoso, A.; Martínez-Esnaola, J.M. Fatigue crack propagation in complex stress fields: Experiments and numerical simulations using the Extended Finite Element Method (XFEM). *Int. J. Fatigue* **2017**, *103*, 112–121. [[CrossRef](#)]
3. Belytschko, T.; Black, T. Elastic crack growth in finite elements with minimal remeshing. *Int. J. Numer. Methods Eng.* **1999**, *45*, 601–620. [[CrossRef](#)]
4. Sukumar, N.; Mões, N.; Moran, B.; Belytschko, T. Extended finite element method for three-dimensional crack modeling. *Int. J. Numer. Methods Eng.* **2000**, *48*, 1549–1570. [[CrossRef](#)]
5. Sukumar, N.; Chopp, D.L.; Moran, B. Extended finite element method and fast marching method for three-dimensional fatigue crack propagation. *Eng. Fract. Mech.* **2003**, *70*, 29–48. [[CrossRef](#)]
6. Patzák, B.; Jirásek, M. Process zone resolution by extended finite elements. *Eng. Fract. Mech.* **2003**, *70*, 957–977. [[CrossRef](#)]
7. Zhang, J.; He, X.D.; Sha, Y.; Du, S.Y. The compressive stress effect on fatigue crack growth under tension–compression loading. *Int. J. Fatigue* **2010**, *32*, 361–367. [[CrossRef](#)]
8. Menouillard, T.; Réthoré, J.; Combescure, A.; Bung, H. Efficient explicit time stepping for the eXtended Finite Element Method (X-FEM). *Int. J. Numer. Methods Eng.* **2006**, *68*, 911–939. [[CrossRef](#)]
9. Fries, T.-P.; Baydoun, M. Crack propagation with the extended finite element method and a hybrid explicit-implicit crack description. *Int. J. Numer. Methods Eng.* **2011**, *89*, 1527–1558. [[CrossRef](#)]
10. Daux, C.; Mões, N.; Dolbow, J.; Sukumar, N.; Belytschko, T. Arbitrary branched and intersecting cracks with the eXtended Finite Element Method. *Int. J. Numer. Methods Eng.* **2000**, *48*, 1741–1760. [[CrossRef](#)]
11. Pathak, H.; Singh, A.; Singh, I.V.; Yadav, S.K. Fatigue crack growth simulations of 3-D linear elastic cracks under thermal load by XFEM. *Front. Struct. Civ. Eng.* **2015**, *9*, 359–382. [[CrossRef](#)]
12. Loehnert, S.; Mueller-Hoeppe, D.S.; Wriggers, P. 3D corrected XFEM approach and extension to finite deformation theory. *Int. J. Numer. Methods Eng.* **2011**, *86*, 431–452. [[CrossRef](#)]
13. Sutula, D.; Kerfriden, P.; Van Dam, T.; Bordas, S.P.A. Minimum energy multiple crack propagation. Part-II: Discrete solution with XFEM. *Eng. Fract. Mech.* **2018**, *191*, 225–256. [[CrossRef](#)]
14. Fleck, N.A.; Shin, C.S.; Smith, R.A. Fatigue crack growth under compressive loading. *Eng. Fract. Mech.* **1985**, *21*, 173–185. [[CrossRef](#)]
15. Sahouryeh, E.; Dyskin, A.V.; Germanovich, L.N. Crack growth under biaxial compression. *Eng. Fract. Mech.* **2002**, *69*, 2187–2198. [[CrossRef](#)]
16. Nikfam, M.R.; Zeinoddini, M.; Aghebati, F.; Arghaei, A.A. Experimental and XFEM modelling of high cycle fatigue crack growth in steel welded T-joints. *Int. J. Mech. Sci.* **2019**, *154*, 178–193. [[CrossRef](#)]
17. Teng, Z.H.; Liao, D.M.; Wu, S.C.; Sun, F.; Chen, T.; Zhang, Z.B. An adaptively refined XFEM for the dynamic fracture problems with micro-defects. *Theor. Appl. Fract. Mech.* **2019**, *103*, 102255. [[CrossRef](#)]
18. Mazlan, S.; Yidris, N.; Kolor, S.S.R.; Petrú, M. Experimental and numerical analysis of fatigue life of aluminum Al 2024-T351 at elevated temperature. *Metals* **2020**, *10*, 1581. [[CrossRef](#)]
19. Abdollahnia, H.; Alizadeh Elizei, M.H.; Reza Kashyzadeh, K. Multiaxial fatigue life assessment of integral concrete bridge with a real-scale and complicated geometry due to the simultaneous effects of temperature variations and sea waves clash. *J. Mar. Sci. Eng.* **2021**, *9*, 1433. [[CrossRef](#)]
20. Ou, M.; Cao, W. On the mechanic performance of building-purpose Q235 steel under high-temperature (Fire). *J. Zhuzhou Inst. Technol.* **2006**, 99–101.
21. Xiao, M. Testing for paris coefficients C_m and ΔK_{th} of Q235. *J. Mech. Strength.* **2003**, *2*, 215–218. [[CrossRef](#)]
22. Jin, S.; Zhang, W. Analysis and verification for the crack growth of lower-wing panel based on XFEM. *J. Xi'an Aeronaut. Inst.* **2023**, *41*, 18–23. [[CrossRef](#)]
23. He, L.; Liu, Z.; Gu, J.; Wang, J.; Men, K. Fatigue crack propagation path and life prediction based on XFEM. *J. Northwest. Polytech. Univ.* **2019**, *37*, 737–743. [[CrossRef](#)]
24. Wang, Z. Crack Propagation of Coiled Tubing Based on Extended Finite Element Method. Master's Thesis, Yangtze University, Jingzhou, China, 2019.
25. Li, Q. Aeroengine Turbine Disk GH4133B Alloy Fatigue Crack Propagation Numerical Simulation Study. Master's Thesis, Xiangtan University, Xiangtan, China, 2018.
26. Melenk, J.; Babuska, I. The partition of unity finite element method: Basic theory and applications. *Comput. Methods Appl. Mech. Eng.* **1996**, *139*, 289–314. [[CrossRef](#)]
27. Sukumar, N.; Chopp, D.L.; Mões, N.; Belytschko, T. Modelling holes and inclusions by level sets in the extended finite element method. *Comput. Methods Appl. Mech. Eng.* **2001**, *190*, 6183–6200. [[CrossRef](#)]
28. Ventura, G.; Budyn, E.; Belytschko, T. Vector level sets for description of propagating cracks in finite elements. *Int. J. Numer. Methods Eng.* **2003**, *58*, 1571–1592. [[CrossRef](#)]

29. Gledić, I.; Mikulić, A.; Parunov, J. Improvement of the ship emergency response procedure in case of collision accident considering crack propagation during salvage period. *J. Mar. Sci. Eng.* **2021**, *9*, 737. [[CrossRef](#)]
30. Killpack, M.; Abed-Meraim, F. Limit-point buckling analyses using solid, shell and solid–shell elements. *J. Mech. Sci. Tech.* **2011**, *25*, 1105–1117. [[CrossRef](#)]

Disclaimer/Publisher’s Note: The statements, opinions and data contained in all publications are solely those of the individual author(s) and contributor(s) and not of MDPI and/or the editor(s). MDPI and/or the editor(s) disclaim responsibility for any injury to people or property resulting from any ideas, methods, instructions or products referred to in the content.